Monthly Notices
of the
ROYAL ASTRONOMICAL SOCIETY

MNRAS **480,** 1353–1362 (2018)
Advance Access publication 2018 June 30

doi:10.1093/mnras/sty1706

Neutron star bulk viscosity, 'spin-flip' and GW emission of newly born magnetars

S. Dall'Osso,[1★] L. Stella[2] and C. Palomba[3]
[1]*Department of Physics and Astronomy, Stony Brook University, Stony Brook 11579 NY, USA*
[2]*INAF – OAR, via di Frascati 33, Monte Porzio Catone, I-00078 Roma, Italy*
[3]*INFN, Sezione di Roma, P.le A. Moro, 2, I-00185 Roma, Italy*

Accepted 2018 June 26. Received 2018 June 26; in original form 2017 October 11

ABSTRACT

The viscosity-driven 'spin-flip' instability in newly born magnetars with interior toroidal magnetic fields is re-examined. We calculate the bulk viscosity coefficient (ζ) of cold, $npe\mu$ matter in neutron stars (NS), for selected values of the nuclear symmetry energy and in the regime where β-equilibration is slower than characteristic oscillation periods. We show that: (i) ζ is larger than previously assumed and the instability time-scale correspondingly shorter; (ii) for a magnetically induced ellipticity $\epsilon_B \lesssim 4 \times 10^{-3}$, typically expected in newborn magnetars, spin-flip occurs for initial spin periods $\lesssim$2–3 ms, with some dependence on the NS equation of state (EoS). We then calculate the detectability of GW signals emitted by newborn magnetars subject to 'spin-flip', by accounting also for the reduction in range resulting from realistic signal searches. For an optimal range of $\epsilon_B \sim (1-5) \times 10^{-3}$, and birth spin period $\lesssim$2 ms, we estimate an horizon of $\gtrsim$4, and $\gtrsim$30 Mpc, for Advanced and third generation interferometers at design sensitivity, respectively. A supernova (or a kilonova) is expected as the electromagnetic counterpart of such GW events. Outside of the optimal range for GW emission, EM torques are more efficient in extracting the NS spin energy, which may power even brighter EM transients.

Key words: dense matter – equation of state – gravitational waves – magnetic fields – stars: magnetar – supernovae: general.

1 INTRODUCTION

The first detections of GWs from binary black holes (BHs; Abbott et al. 2016, Abbott et al. 2017a) and from a binary neutron stars (NS) merger (Abbott et al. 2017d) have opened a new era in physics and astronomy. Newly born magnetars have long been discussed as a class of compact objects of potential relevance for current and future GW detectors (Cutler 2002, Stella et al. 2005, Corsi & Mészáros 2009, Dall'Osso, Shore & Stella 2009, Dall'Osso et al. 2015).

The ability of newborn magnetars to emit a distinctive GW signal, the properties of such signals, and their rate of occurrence, are sensitive to the NS properties; therefore, they hold the potential to probe the physics of NS interiors. Cutler (2002) first pointed out that millisecond spinning NS with predominantly toroidal interior B-fields, for example, magnetars, may be subject to a secular instability first discussed by Jones (1976), which favors intense GW emission. Schematically,[1] a strong toroidal field deforms the NS shape into a prolate ellipsoid, which undergoes freebody precession. Dissipation of the precession energy, due to the NS interior viscosity, will drive the symmetry (magnetic) axis of the ellipsoid orthogonal to the spin axis, thus maximizing GW emission efficiency. This is often referred to as[2] 'spin-flip instability'; the *prolate* shape of the ellipsoid, induced by a strong *toroidal* magnetic field in the NS core, is essential for the instability.

The B-field strength in magnetar cores can only be inferred from observations of the galactic population. Based on the energetics of the 2004 December 27 Giant Flare of the Soft Gamma Repeater SGR 1806-20, Stella et al. (2005) derived a lower limit $\sim 10^{16}$ G for the volume-averaged B-field *at birth*. Makishima et al. (2014), based on the possible precession of the Anomalous X-ray Pulsar 4U 0142+61, estimated B $\sim 10^{16}$ G at $\sim 10^4$ yr age. Such magnetic field in the core of newborn magnetars would give rise to GW signals detectable from well beyond the Milky Way.

Key to strong GW emission is that flipping of the symmetry axis be fast compared to other mechanisms like, for example, magnetic dipole radiation, that tap the same energy reservoir as GWs, *i.e.*

★ E-mail: sim.dall@gmail.com

[1] see Cutler (2002) and Jones (1976) for more details.

[2] Even though, in the observer's frame, it is the magnetic symmetry axis that flips.

Published by Oxford University Press on behalf of the Royal Astronomical Society

the NS spin. Thus, an effective source of viscosity is crucial. To further study this scenario, Dall'Osso et al. (2009) considered bulk viscosity in pure *npe* NS matter soon after birth, at temperatures $\sim 10^{10}$ K, when the NS crust has not yet formed.

These authors concluded that: (i) for birth spin ∼1–3 ms, the instability is sufficiently fast if the interior B-field is[3] $B_{\rm int,\,16} \lesssim 4$ and the exterior dipole $B_{\rm d,\,14} \lesssim 5$; (ii) GW signals are detectable with Advanced LIGO/Virgo from Virgo cluster distances. Given an estimated magnetar formation rate $\sim 1\ {\rm yr}^{-1}$ within that volume, this may lead to an interesting rate of detectable events, in particular, for $B_{\rm int,\,16} \gtrsim 1$, $B_{\rm dip,\,14} < 3$, and birth spin periods <2.5 ms.

Here, we improve on previous work in several ways: In Section 2, we calculate the bulk viscosity coefficient of *npeμ* matter, for three representative choices of the NS equation of state (EoS), showing that it is generally larger than previously assumed. In passing, we address doubts raised about the effectiveness of bulk viscosity. In Section 3, we summarize the formalism used to model spin-flip as a consequence of viscous dissipation of freebody precession, and calculate numerically the time evolution of the tilt angle of the magnetic axis, along with the corresponding GW luminosity. In Section 4, using our new results, we re-asses the detectability of newborn magnetars with current and future GW detectors, and further comment on perspectives for the detection of associated EM signals.

2 BULK VISCOSITY IN THE NS CORE

Fluid bulk viscosity is due to pressure/density variations from equilibrium. In a precessing NS, such fluctuations are excited at the precession frequency. In β-stable NS matter, pressure depends on the local density *and* charged particle fraction: when a fluid element is displaced from equilibrium, the ensuing compression will activate β-reactions, to establish a new pressure and chemical equilibrium. Bulk viscosity is thus characterized by two time-scales: the perturbation period, $T_{\rm p} = 2\pi/\omega$, equal to the precession period, and the relaxation time-scale $\tau_\beta = 2\pi/\omega_\beta$, on which chemical equilibrium is restored. For *npe* matter, the bulk viscosity coefficient is[4] (Lindblom & Owen 2002)

$$\mathrm{Re}(\zeta) \equiv \frac{n_{\rm b}\tau_\beta \left(\dfrac{\partial P}{\partial x}\right)_{n_{\rm b}} \dfrac{{\rm d}x}{{\rm d}n}}{1+(\omega\tau_\beta)^2} = \frac{z}{1+z^2}\,\frac{n_{\rm b}}{\omega}\left(\frac{\partial P}{\partial x}\right)_{n_{\rm b}}\frac{{\rm d}x}{{\rm d}n_{\rm b}}. \tag{1}$$

where P, n_b are the total pressure and baryon density, $z = \omega\tau_\beta$ and $x = n_{\rm p}/n_{\rm b}$ the proton fraction. Equation (1) highlights the dependence of bulk viscosity on the perturbation frequency, chemical composition, density, and pressure profiles of the NS structure.

The different regimes – equation (1) has two main regimes of ζ as a function of z:

i) $z \ll 1$, 'low frequency' limit. Chemical equilibrium is established quickly compared to the perturbation period ($T_{\rm p}$). Thus, deviations from chemical equilibrium cannot grow much and energy losses remain very limited, resulting in a small bulk viscosity coefficient, which scales like $\zeta \propto z$;

ii) $z \gg 1$, 'high frequency' limit. Chemical imbalance is erased over a time much longer than the perturbation period. During each cycle, deviations from chemical equilibrium grow *almost* freely: the small dissipation due to β-reactions builds up only in a large number of cycles, eventually damping the perturbation. In this regime $\zeta \propto z^{-1}$.

Table 1. Different choices for the symmetry energy S_v and power-law index γ. Case *I* matches closely the results for the APR EoS. Cases *II* and *III* are for illustration purposes.

CASE	S_v[MeV]	γ	S_v[MeV]	Γ
I	15.5	1/2	32.5	0.59
II	14.5	1/3	31.5	0.525
III	13.5	1/4	30.5	0.503

These two regimes join smoothly around $z \sim 1$, where the bulk viscosity coefficient $\zeta(z)$ reaches a maximum.

Standard expression – $z \gg 1$ is typically the relevant regime in NS (e.g. Haensel, Levenfish & Yakovlev 2000, 2001, Lindblom & Owen 2002, Dall'Osso et al. 2009), unless $T > 10^{10}$ K. In particular, assuming a NS made of pure *npe* matter, and treating each particle species as a fluid of non-interacting, fully degenerate fermions, the standard expression for the bulk viscosity coefficient (Sawyer 1989) can be derived from equation (1) for $z \gg 1$

$$\zeta^{\rm (std)} \approx 6 \times 10^{-59}\rho^2 T^6 \omega^{-2}. \tag{2}$$

Equation (2) can be improved in two ways: (i) a more realistic description of NS matter, which accounts for the interactions among baryons, by specifying the NS EoS; (ii) the inclusion of additional particles, expected to appear in the NS core at large densities (e.g. Haensel et al. 2000, Lindblom & Owen 2002). Muons will be first produced in β-reactions once the electron Fermi energy exceeds the muon rest-mass ≈105 MeV. The exact density threshold for muon production depends on the NS EoS and has a typical value $\rho \lesssim 2.3 \times 10^{14}\ {\rm g\,cm^{-3}}$. We will not consider further particles, that might appear in the core at $\rho > 8 \times 10^{14}\ {\rm g\,cm^{-3}}$.

2.1 Nuclear symmetry energy

Baryon interactions in the NS EoS are described in terms of $E_N(n_{\rm b}, x)$, the nucleon energy per baryon, at baryon number density $n_{\rm b} = n_n + n_{\rm p}$. If $\mathrm{E}_N(n_{\rm b}, 0)$ is the energy of pure neutron matter and $E_N(n_{\rm b}, 1/2)$ the energy of symmetric matter, then the former exceeds the latter by the symmetry energy, $S_0(n_{\rm b})$. For intermediate x-values, the excess energy is obtained interpolating between these two limits

$$\mathrm{E}_N(n_{\rm b}, x) \approx \mathrm{E}_N(n_{\rm b}, 1/2) + S_0(n_{\rm b})(1-2x)^2. \tag{3}$$

$S_0(n_{\rm b})$ has a kinetic and a potential energy component

$$S_0(u) = S_k u^{2/3} + S_v u^\gamma, \tag{4}$$

the latter incorporating baryons interactions. In equation (4), $u = n_{\rm b}/n_{\rm s}$, $n_{\rm s} \approx 0.16\ {\rm fm}^{-1}$ is the baryon number density at the nuclear saturation density $\rho_s \approx 2.7 \times 10^{14}\ {\rm g\,cm^{-3}}$, $S_k = 17$ MeV and $S_k + S_v = S_0(u_s)$. The index $\gamma \sim 0.2$–1 (Steiner, Lattimer & Brown 2010) parametrizes the uncertain scaling of the potential energy with density. equation (4) is often written as $S_0(n_{\rm b}) = S_v (n_{\rm b}/n_s)^\Gamma$, where $S_v = S_k + S_v \sim 30$–34 MeV positively correlates with $\Gamma \sim 0.45$–0.7 (Lattimer & Prakash 2016). Here, we consider three representative choices of (S_v, γ) that span the range of uncertainty on both parameters: chosen values are reported in Table 1. Case *I* gives a relatively stiff EoS approximating the APR EoS (Akmal, Pandharipande & Ravenhall 1998). Cases *II* and *III* give a progressively softer EoS, consistent with a NS maximum mass $\gtrsim 2\,{\rm M}_\odot$ (e.g. Demorest et al. 2010).

---

[3] From here on, $Q_n \equiv Q/10^n$.

[4] Equation (1) is valid for any fluid with relativistic components. For practical purposes, in the case of *npeμ* matter, we will adopt a slightly different expression which is derived from equation (1).

2.2 Charged particle fraction

Accounting for baryon interactions increases the charged particle fraction with respect to the simple case with no interactions.

Case 1. npe matter – the total energy per baryon inside a NS includes, besides E_N, the energy of relativistic electrons, $\mathrm{E}_e = 3/4xE_{F_e} = (3/4)\hbar cx(3\pi^2 n_\mathrm{b}x)^{1/3}$, with $x = x_e = x_p$ due to charge neutrality. The equilibrium composition is obtained by minimizing the total energy with respect to x, $\partial[E_N(n_\mathrm{b}, x) + E_e(n_\mathrm{b}, x)]/\partial x = 0$, which is equivalent to imposing the equality of the chemical potentials, $\mu_e = \mu_n - \mu_p$

$$\hbar c\left(3\pi^2 n_\mathrm{b}x\right)^{1/3} = -\frac{\partial E_N}{\partial x} = 4S_v\left(\frac{n_\mathrm{b}}{n_\mathrm{s}}\right)^\Gamma (1-2x). \tag{5}$$

Solving equation (5) gives the proton fraction in the NS core: for example, at the nuclear saturation density, $x(n_\mathrm{s}) \approx 0.04$ for all EoS considered, as opposed to $x(n_\mathrm{s}) \approx 0.006$ obtained in the non-interacting case.

Case 2. npeμ matter – : the appearance of muons introduces new constraints. First, the electron and muon chemical potentials must be equal. Secondly, x_e and x_p will appear as different variables in equation (5), since now x_p must equal the sum of the electron and muon fractions. The e, μ, and p fractions are determined from

$$\begin{aligned}\mu_e &= \mu_n - \mu_p\\ \mu_\mu &= \mu_e\\ x_p &= x_e + x_\mu.\end{aligned} \tag{6}$$

The profiles $x_p(n_\mathrm{b})$, $x_e(n_\mathrm{b})$ and $x_\mu(n_\mathrm{b})$, corresponding to the three EoS's of Table 1 are shown Fig. 1. The threshold for muons production is $\rho_\mu \approx 2.5 \times 10^{14}\,\mathrm{g\,cm^{-3}}$: below ρ_μ, $x_\mu = 0$ while $x_p = x_e$ is determined by equation (5). Where muons appear, the proton fraction is increased. Accordingly, the threshold for the onset of direct URCA reactions is reached at a somewhat lower density ($\gtrsim 9 \times 10^{14}\,\mathrm{g\,cm^{-3}}$).

2.3 Relaxation time-scale

The relaxation time-scale, in the same approximation that gives equation (2), is (Reisenegger & Goldreich 1992)

$$\tau_\beta^{(\mathrm{old})} = \frac{3n_c}{\lambda E_{F_\mathrm{n}}} \approx 6.9\mathrm{s}\,(\rho/\rho_\mathrm{n})^{2/3}\,T_{10}^{-6}, \tag{7}$$

where λ is related to the emissivity of modified Urca reactions and $\mathrm{E}_{F_\mathrm{n}}$ is the neutron Fermi energy. Including $S(n_\mathrm{b}, x)$ decreases τ_β, which, in turn, increases ζ compared to equation (2). In order to derive the relaxation time-scale in this case let us assume, for example, a density perturbation in a fluid element, which will thus find itself out of chemical equilibrium by the amount $\delta\mu = \mu_n - \mu_p - \mu_e$. This is related to δn_c, the deviation of the charged particle density from its equilibrium value (equation 5). β-reactions will be activated, in order to bring n_c to its new equilibrium value and restore chemical equilibrium ($\delta\mu = 0$). The relaxation time-scale is, as usual, $\tau_\beta = \delta n_c/\delta\Gamma$, where $n_c = n_\mathrm{p} = n_e$, and $\delta\Gamma = \lambda\delta\mu$ is[5] the difference in the rates between direct and inverse β-reactions. Perturbing equation (5) with respect to x, we get

$$\tau_\beta \equiv \frac{3n_c}{\lambda\left[E_{F_\mathrm{n}} + 24S_v x(n_\mathrm{b}/n_\mathrm{s})^\gamma\right]}. \tag{8}$$

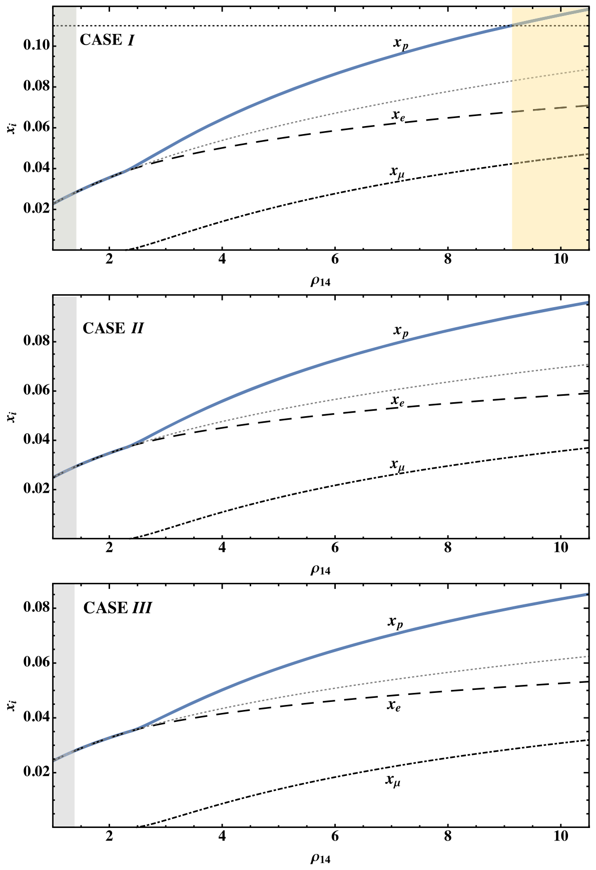

Figure 1. Proton, electron and muon fractions for the three cases in Table 1. *Upper Panel*: the horizontal dotted line is the x_p threshold for direct Urca reactions. It is not reached in cases *II* and *III*. In the yellow area direct Urca reactions are allowed, hence our calculations should be modified. The grey area on the left corresponds to densities of the NS crust.

which generalizes equation (7). The symmetry energy term in the denominator is typically $\gtrsim 0.5\ \mathrm{E}_{F_\mathrm{n}}$, which reduces τ_β in *npe* by a factor 1.5 compared to $\tau_\beta^{(\mathrm{old})}$.

Allowing for the presence of muons, and accounting for the contribution of the proton branch of different β-reactions, provides another factor ~2 reduction (Haensel, Levenfish & Yakovlev 2001). We thus conclude that $\tau_\beta \simeq 1/3\tau_\beta^{(\mathrm{old})}$ for *npeμ* matter.

2.4 Total energy and pressure profile

The total energy per baryon, for *npeμ* matter, is $\mathrm{E}_T(n_\mathrm{b}, x_p) = E_N(n_\mathrm{b}, x_p) + 3/4x_eE_e(n_\mathrm{b}, x_p) + 3/4x_\mu E_\mu(n_\mathrm{b}, x_p)$, where E_μ is the equivalent of E_e. The total pressure is $P(n_\mathrm{b}, x_p) = P_N(n_\mathrm{b}, x_p) + P_e + P_\mu$, where P_e, P_μ are the partial pressures of the free lepton gases. The nucleon pressure is defined as

$$P_N(n_\mathrm{b}, x_p) = n_\mathrm{b}^2\frac{\partial E_\mathrm{N}(n_\mathrm{b}, x_p)}{\partial x}. \tag{9}$$

$p = n^2\partial[E(n, x) + E_e(n, x)]/\partial x$. Summing P_e and P_μ to equation (9) gives the total pressure as a function on n_b and x, needed to calculate $(\partial P/\partial x)_n$ in equation (1).

2.5 Bulk viscosity coefficient of *npeμ* matter

When several particles species are present, the formulation by Haensel et al. (2001) turns out to be more practical to calculate

---

[5] Under the assumption that $\delta\mu \ll kT$.

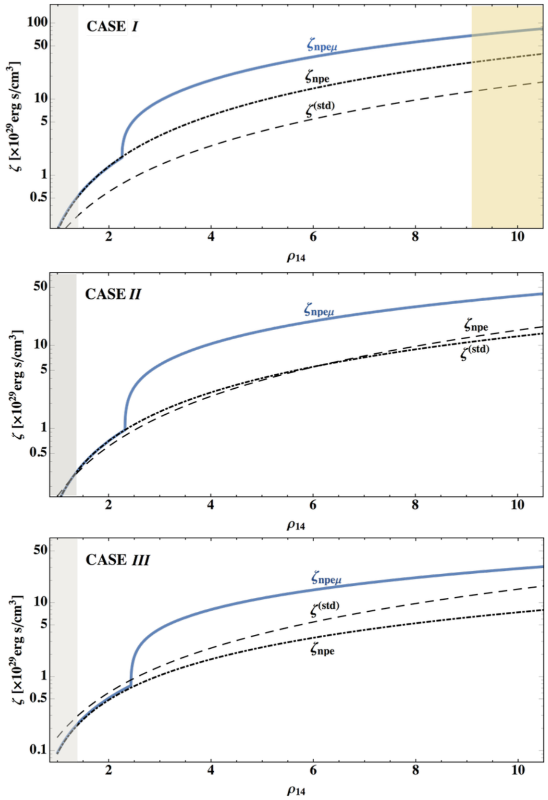

Figure 2. Bulk viscosity coefficient for $npe\mu$ NS matter (blue), for the three cases of Section 2.1. The curves marked ζ_{npe} represent the coefficient calculated without muons, those marked $\zeta^{\rm (std)}$ are from the 'standard' expression (equation 2). The grey and yellow shaded areas are as in Fig. 1. From top to bottom, the density-averaged value of ζ is about 5, 3, and 2 times larger than that derived from equation (2).

ζ than that of equation (1). We write the total bulk viscosity as the sum of partial bulk viscosities[6] due to each of the channels for β-reactions. Thus, $\zeta = \zeta_{ne} + \zeta_{pe} + \zeta_{n\mu} + \zeta_{p\mu}$, where

$$\zeta_{Nl} = \frac{\lambda_{Nl}}{\omega^2} \left|\frac{\partial P}{\partial x}\right|_{n_{\rm b}} \frac{dx}{dn_{\rm b}} = \frac{|\lambda_{Nl}|}{\omega^2} C_l^2, \tag{10}$$

Nl standing for each nucleon/lepton couple. The term $C_l \equiv n_{\rm b} \partial \eta_l / \partial n_{\rm b}$, where $\eta_l = \mu_n - \mu_p - \mu_l$ is the chemical potential imbalance of leptons, and the λ's for each branch of modified URCA reactions are given by Haensel et al. (2001). The neutron/proton chemical potentials are $\mu_{n,p} = \partial(n_{\rm b} E_N)/\partial n_{n,p}$. For the leptons, $\mu_l = \left(m_l^2 c^4 + p_{Fl}^2 c^2\right)^{1/2}$, where $p_{Fl} = \hbar \left(3\pi^2 n_l\right)^{1/3}$ is the Fermi momentum.

With these definitions, C_l becomes (Haensel et al. 2000)

$$\begin{aligned} C_l &= -n_{\rm b} \frac{\partial^2 E_N(n_{\rm b}, x_p)}{\partial n_{\rm b} \partial x_p} - \frac{c^2 p_{Fl}^2}{3\mu_l} \\ &= \left(1 - 2x_p\right) n_{\rm b} \frac{d}{dn_{\rm b}} \left(\frac{\mu_l}{1 - 2x_p}\right) - \frac{c^2 p_{Fl}^2}{3\mu_l}, \end{aligned} \tag{11}$$

where equation (4) has been used in the last step. We adopted equation (11) to calculate the bulk viscosity coefficient of $npe\mu$ matter, for the three EoS's discussed in Section 2.1. The results are shown in Fig. 2: for each case, the blue curve shows the run of ζ with density, compared with its value in the absence of muons, and with the value given by equation (2). More details are given in the caption.

In all three cases, the resulting bulk viscosity coefficient is greater than the standard one at all densities: their ratio decreases slightly with density for EoS's *II* and *III*, while it is constant for EoS *I* (above the threshold for the appearance of muons). Assuming a NS with a 12 km radius and 1.4 $M_\odot$ mass, the density-averaged values of ζ for the three EoS's considered here are, respectively, ~5, 3, and 2 times larger than the density-averaged value of equation (2). These ratios represent a convenient parametrization of the effective increase of NS bulk viscosity, for the EoS's and chemical compositions considered here, and will be adopted in the following.

3 'SPIN-FLIP'

We can now calculate the time evolution of the tilt angle in newborn magnetars. Most details were worked out by Dall'Osso et al. (2009), based on Mestel & Takhar (1972; see also Lasky & Glampedakis 2016).

NS cooling – We consider modified Urca cooling, that is simply described as (e.g. Page, Geppert & Weber 2006)

$$T_{10}(t) = \left(\frac{t}{20{\rm s}} + \frac{1}{T_{i,10}^6}\right)^{-1/6}, \tag{12}$$

$T_{10} = T/10^{10}$ K being the NS temperature and assuming $T_{i,10} \gtrsim 3$. equation (12) describes hot NS where neither protons nor neutrons are superfluid. Protons become superconducting below $T_{cp,10} \sim 5$, or $t \approx 10^3$ s, while neutrons likely become superfluid at much lower T (and later times; e.g. Page et al. 2011). The transition to proton superconductivity reduces progressively the neutrino emissivity, as T drops below T_{cp}: however, (12) remains approximately valid as long as $T/T_{cp} \gtrsim 0.7$ (cf. Haensel et al. 2001), *i.e.* up $t \sim 10^4$ s.

Magnetically induced ellipticity – As a first approximation, the NS magnetically induced ellipticity is of the order of the ratio of magnetic to gravitational binding energy,

$$\epsilon_B \sim 4 \times 10^{-4} B_{t,16}^2 R_{12}^4 / M_{1.4}^2, \tag{13}$$

where $B_{t,16}$ is the volume-averaged *toroidal* field strength in units of 10^{16} G, R_{12} the NS radius in units of 12 km and $M_{1.4}$ the NS mass, in units of 1.4 $M_\odot$. Corrections due to the magnetic field geometry in the NS interior can lead to substantially larger deformations at a given B-field strength (Bonazzola & Gourgoulhon 1996, Mastrano et al. 2011, Akgün et al. 2013, Dall'Osso et al. 2015). In particular, the toroidal-to-poloidal field ratio is an unknown parameter that can be very large in the core of non-barotropic NS (Braithwaite 2009, Akgün et al. 2013, Ciolfi & Rezzolla 2013). Given these uncertainties, we will adopt $\epsilon_B \approx 10^{-3}$ as a reference value[7] of ϵ_B for a ~10^{16} G toroidal B-field in the NS core. Calling χ the tilt angle of the magnetic symmetry axis to the spin axis, the freebody precession frequency will be $\omega = \Omega \epsilon_B \cos\chi$, with Ω the NS spin frequency.

3.1 Energy dissipation

The energy dissipation rate due to bulk viscosity is

$$\dot{\rm E}_{\rm diss} \equiv \int \zeta\, |\nabla \cdot \delta {\bf v}|^2 \sim \omega^2 \int \zeta\, (\Delta\rho/\rho)^2\, {\rm d}V, \tag{14}$$

---

[6] For $\tau_\beta > T$.

[7] For example, the twisted-torus used in Dall'Osso et al. 2015 has $\epsilon_B \approx 0.9 \times 10^{-3} B_{t,16}^2$, for the same mass and radius used here.

where $\Delta\rho = \delta\rho + \boldsymbol{\xi}\cdot\nabla\rho = -\rho_0\nabla\cdot\boldsymbol{\xi}$ is the Lagrangian density perturbation due to the precessional motion, $\delta\rho$ the corresponding Eulerian perturbation, $\boldsymbol{\xi}$ the displacement field, and $\delta\boldsymbol{v} = \partial_t\boldsymbol{\xi}$ the velocity perturbation.

Fluid compression – Dall'Osso et al. (2009) approximated $\Delta\rho \approx \delta\rho$, adopting $\delta\rho$ as derived by Mestel & Takhar (1972). Lasky & Glampedakis (2016) argued that this approximation only holds if $\omega\tau_\beta < 1$ whereas, if $\omega\tau_\beta > 1$, β-reactions would have no time to occur in one precession cycle, leaving the charged particle fraction unchanged, $\Delta x = 0$; since, to first order in the perturbation, the fluid compression $\nabla\cdot\boldsymbol{\xi} \propto \Delta\rho \propto \Delta x$, this[8] would give $\Delta\rho = 0$, thus quenching bulk viscosity and preventing spin-flip.

By imposing $\omega\tau_\beta \leq 1$, and using the spin-flip time-scale (equation 16), Lasky & Glampedakis (2016) derived a maximum ellipticity $\epsilon_{\rm sf} \approx 5\times10^{-3}\rho_{15}/P^2_{\rm ms}$ for spin-flip to operate ($\mathrm{P}_{\rm ms}$ is the spin period in milliseconds). Repeating their argument with our updated values $\tau_\beta = 1/3\tau_\beta^{\rm (old)}$ and $\zeta = A\zeta^{\rm (std)}$ (Section 2.1 and 2.5), we find $\epsilon_{\rm sf}^{\rm (new)} = A\epsilon_{\rm sf} \approx 1.5\times10^{-2}(\mathrm{A}/3)\rho_{15}/P^2_{\rm ms}$. The mechanism can thus operate on a wider range of ellipticities than previously suggested: constraints on ϵ_B based on short gamma-ray burst (GRB) observations should be accordingly revised.

The above argument is still approximate, since it (i) uses the simple scaling (16), (ii) has an explicit dependence on ρ, and (iii) assumes a sharp cut-off of bulk viscosity at $\omega\tau_\beta = 1$. To improve on these points, we use the definition of the dissipation time-scale (equation 15), integrating it over the NS density profile, and introduce a slight modification in the treatment of fluid compressibility. First note that τ_β defines the characteristic time-scale for β-reactions in a perturbed fluid element. Because a large number of such reactions per unit volume ($\sim\delta n_c$) must occur in the time τ_β, a fraction $\sim t/\tau_\beta$ of those reactions must occur in a time interval $t < \tau_\beta$, causing some energy dissipation. Consider now a perturbation with the period $T_{\rm p} < \tau_\beta$. The charged particle fraction will change by an amount that is $\sim T_{\rm p}/\tau_\beta$ times smaller than when $T_{\rm p} > \tau_\beta$, and we expect $\Delta\rho$ to be $\sim T_{\rm p}/\tau_\beta$ smaller than in the long time-scale regime, where it was $\approx\delta\rho$. Thus, when $\tau_\beta > T_{\rm p}$ we assume the relation $\Delta\rho \approx \delta\rho(T_{\rm p}/\tau_\beta)$: the decreasing efficiency of β-reactions provides a force that opposes compression but, as long as $T_{\rm p} \approx \tau_\beta$, cannot prevent it altogether.

To summarize, depending on the bulk viscosity regime we will write: (i) $\Delta\rho \approx \delta\rho$ ($\omega\tau_\beta \leq 1$, highly compressible fluid); (ii) $\Delta\rho = \delta\rho(T_{\rm p}/\tau_\beta)$ in the opposite limit ($\omega\tau_\beta > 1$). Note that, because the integral in equation (14) contains the square of $\Delta\rho$, energy dissipation becomes quickly negligible as $\tau_\beta > T_{\rm p}$. Thus, our expression models the onset of fluid incompressibility as a smooth, yet fast transition that occurs, as the NS cools, in a narrow region around $\omega\tau_\beta \gtrsim 1$.

3.2 Dissipation time-scale

The energy dissipation time-scale is (Ipser & Lindblom 1991)

$$\tau_{\rm diss} \equiv \frac{2E_{\rm pre}}{\dot{E}_{\rm diss}} = \frac{I}{\epsilon_B}\frac{1}{\displaystyle\int \zeta\left(\frac{\Delta\rho}{\rho}\right)^2 {\rm d}V}, \tag{15}$$

where, to first order in ϵ_B, the freebody precession energy is $\mathrm{E}_{\rm pre} = 1/2I\Omega^2\epsilon_B\cos^2\chi = 1/2I\omega^2\epsilon_B^{-1}$ (Dall'Osso et al. 2009). A simple dimensional analysis of equation (15) gives the scaling of $\tau_{\rm diss}$ with the NS parameters:

$$\tau_{\rm diss} \sim \frac{2\rho R^2}{5\epsilon_B\epsilon_\Omega^2\zeta}, \tag{16}$$

where the integral in equation (15) is substituted by a volume-averaged bulk viscosity times a volume-averaged rotational deformation $\epsilon_\Omega \sim \Omega^2 \sim \delta\rho/\rho$, and the NS moment of inertia as that of a uniform density sphere.

We note some implications of Equations 16: (i) $\tau_{\rm diss} \sim \zeta^{-1}$: larger(smaller) values of the bulk viscosity coefficient imply a shorter(longer) dissipation time. Note that, since $\zeta \sim T^6$, the tilt angle evolution is very sensitive to the NS cooling history; (ii) $\tau_{\rm diss} \sim \epsilon_B$, since $\zeta \sim \epsilon_B^{-2}$: the dissipation time is thus longer for larger ellipticities; (iii) $\tau_{\rm diss} \gg T_{\rm p} \approx \mathrm{P}_{\rm ms}/(\epsilon_{B,-3}\cos\chi)$ s: damping takes a large number of cycles, unless $\chi \approx \pi/2$.

3.3 Tilt angle growth time

The growth time of the tilt angle, τ_χ, is defined as

$$\tau_\chi = \frac{\sin\chi}{\dfrac{\rm d}{{\rm d}t}\sin\chi} = \frac{\sin\chi}{\dot{\chi}\cos\chi} \tag{17}$$

from which, using the expression for $\mathrm{E}_{\rm pre}$ and its time derivative, we obtain (Dall'Osso et al. 2009)

$$\tau_\chi = \frac{\sin^2\chi}{\cos^2\chi}\tau_{\rm diss}. \tag{18}$$

Combining these two expressions, the evolution equation for the tilt angle is readily obtained.

3.4 Tilt angle evolution

For each of the three EoS's of Section 2.1, and assuming a *npeμ* composition, we calculated the integral in equation (15) numerically, as described in detail by Dall'Osso & Perna (2017), *i.e.* following the change of $\Delta\rho$ described in Section 3.1 as the NS switches from the low-frequency to the high-frequency regime of bulk viscosity. For millisecond spin periods and ellipticities $\epsilon_B \sim 10^{-3}$, as expected in newly born magnetars, bulk viscosity enters the high-frequency regime at temperatures $\lesssim 10^{10}$ K. The resulting expressions for $\tau_{\rm diss}$ have been used to calculate the temporal evolution of χ.

3.4.1 *Coupled tilt angle and spin evolution*

Since $\tau_{\rm diss}$ depends on the precession frequency, hence on the NS spin, the evolution equations for χ and Ω are formally coupled. Dall'Osso et al. (2009) solved the equation for $\chi(t)$ under the assumption of a constant Ω, i.e. that spin-flip was much faster than the initial spin-down due to the magnetic dipole. Here, we extend their treatment, by adopting the newly derived expression for $\tau_{\rm diss}$ and solving the coupled evolution equations for $\chi(t)$ and $\Omega(t)$, without restrictions on the relation between the spin-flip and magnetic dipole spin-down time-scales.

---

[8] This proportionality holds strictly to first-order (Mestel & Takhar 1972). Studying higher -order terms, Lander & Jones (2017) found that fluid compressibility remains high even as Δx is reduced. Our estimates may thus be regarded as conservative.

3.4.2 Numerical solutions

We obtain the evolution equation for the spin frequency by considering that the NS spin energy is extracted by two mechanisms : (i) magnetic dipole radiation – which acts right after the NS is born – at the rate (e.g. Spitkovsky 2006)

$$\dot{\mathrm{E}}_{\mathrm{EM}} = -\frac{\mu^2 \Omega^4}{c^3} \left(1 + \sin^2 \chi\right) , \tag{19}$$

where $\mu = \mathrm{B_d} R^3/2$ is the NS magnetic moment, $\mathrm{B_d}$ the dipole field strength at the magnetic pole and χ the tilt angle of the dipole field to the spin axis (assumed to be equal to the tilt of the axis of the interior toroidal field); (ii) GW emission, at the rate (Jones & Andersson 2001)

$$\dot{\mathrm{E}}_{\mathrm{GW}} = -\frac{2}{5}\frac{\mathrm{G}}{c^5} \left(I \epsilon_B\right)^2 \Omega^6 \sin^2\chi \left(1 + 15 \sin^2 \chi\right) ; \tag{20}$$

we set $\sin^2 \chi \left(1 + 15 \sin^2 \chi\right) \equiv \hat{F}(\chi)$ for later use.

The differential equation for Ω will thus be

$$\dot{\Omega} = \left(\dot{\mathrm{E}}_{\mathrm{GW}} + \dot{\mathrm{E}}_{\mathrm{EM}}\right) / I \Omega . \tag{21}$$

Tilt angle distribution at $t = 10^3$ s – By combining equations 21 and 18, and using equation (15) for τ_{diss}, we can calculate the numerical solutions for $\chi(t)$ and $\Omega(t)$ given the NS mass, radius, EoS (hence ζ) and initial conditions (χ_i, $\mathrm{P_{ms,\,i}}$, ϵ_B, $\mathrm{B_d}$). Fig. 3 illustrates results for EoS *II*, with the value of χ at $t = 10^3$ s reported as a function of the initial spin period and NS ellipticity, in three representative cases: (i) in the top panel, a $1.4\,\mathrm{M}_\odot$ NS with a 12 km radius and $\mathrm{B_d} = 6 \times 10^{14}$ G are used; (b) in the middle panel, the same mass and radius are considered, along with a much stronger dipole $\mathrm{B_d} = 5 \times 10^{15}$ G; (c) the bottom panel shows results for an $1.9\,\mathrm{M}_\odot$ NS, with a 10 km radius and $\mathrm{B_d} = 6 \times 10^{14}$ G. Over most of the parameter space, the growth time of the tilt angle is $<$20 s, and in no case it exceeds a few hundred seconds.

In all panels, two regions are apparent: almost orthogonal or nearly aligned rotators, separated by a relatively narrow strip of intermediate cases. The upper and middle panels show clearly that the separation is almost insensitive to the strength of the magnetic dipole field, confirming that spin-flip is, in general, faster than magnetic dipole spin-down (Dall'Osso et al. 2009). The upper and lower panels, on the other hand, show a small, yet noticeable influence of the NS compactness: the more massive and smaller NS tends to dissipate more slowly, resulting in a slightly larger region of aligned rotators in parameter space (see caption for more details). Spin-flip fails in the high-ϵ_B and long $\mathrm{P_{ms}}$ sector of parameter space, owing to the freezing of viscous dissipation when the dissipation time is longer than the cooling time. At birth, both time-scales scale as T^{-6}, so whether this condition is realized or not is determined by initial values of ϵ_B and $\mathrm{P_{ms}}$. Once the switch to the high-frequency regime of bulk viscosity has completed, τ_{diss} becomes even more sensitive to T, progressively freezing the value of the tilt angle. Since, in this regime, the dissipation time is $\sim\epsilon_B$, large-ellipticity NSs are those mostly affected by the freezing.

The density-averaged bulk viscosity coefficient for EoS *II* is $\approx$3 times larger than the value in equation (2). For EoS *I*, it is almost twice as strong, making an even larger region of parameter space accessible to orthogonal rotators. For EoS *III*, it is just 2/3 of the one adopted in Fig. 3, leading to a small reduction of the interesting parameter range.

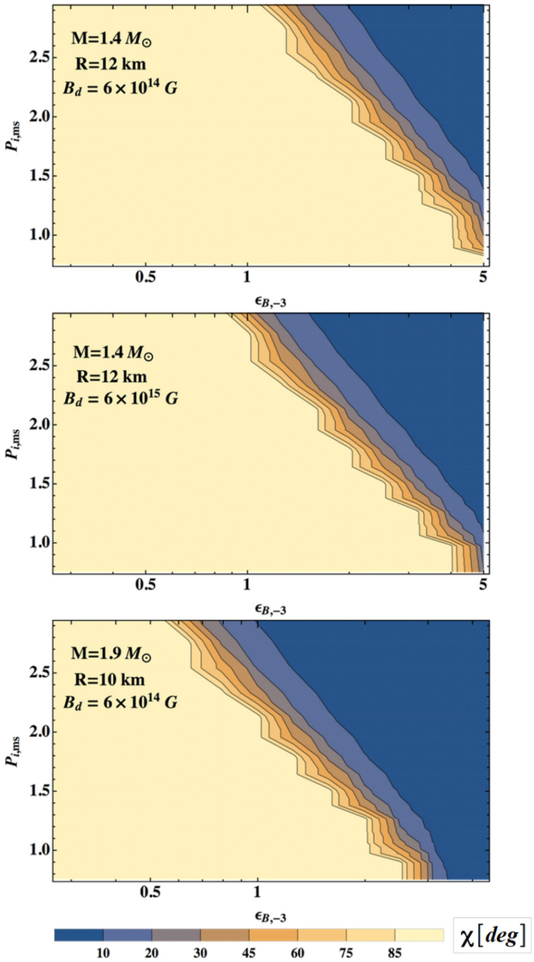

Figure 3. Tilt angle χ, calculated at $t \gtrsim 10^3$ s, as a function of the initial spin and magnetically induced ellipticity, for EoS *II* and three different NS parameter combinations (shown in the plots). The parameter space is divided in two by a relatively narrow strip: most magnetars end up either as almost orthogonal (yellow area, left) or almost aligned (blue area, right-hand side) rotators. A larger magnetic dipole (*middle panel*) has a minor impact demonstrating that spin-flip, when it occurs, is faster than the EM spin-down. A larger mass, on the other hand, effectively delays spin-flip, slightly reducing the range in parameter space occupied by large tilt angles (*lower panel*). In the upper panel, the relation $P_{\mathrm{ms}} < -3.33 \log_{10} \epsilon_{B,\,-3} + 3.23$ approximates the dividing line at $\chi \approx 60°$. Similarly, for the middle and lower panels we obtain, respectively, $P_{\mathrm{ms}} < -3.1 \log_{10} \epsilon_{B,\,-3} + 2.85$ and $P_{\mathrm{ms}} < -3.23 \log_{10} \epsilon_{B,\,-3} + 2.27$.

4 GW AND EM TRANSIENTS

The NS spin energy is $\mathrm{E_{spin}} = (1/2) I \Omega^2$. The moment of inertia can be well approximated by the polynomial[9] (Lattimer & Prakash 2016)

$$I \approx M R^2 \left(0.247 + 0.642\beta + 0.466\beta^2\right) , \tag{22}$$

as a function of the compactness $\beta = GM/(c^2 R)$. Because the maximum NS spin frequency is also expressed by a nearly universal relation (Lattimer & Prakash 2016),

$$\nu_{\max} \approx 1.08\,\mathrm{kHz} \left(\frac{M}{1.4\,\mathrm{M}_\odot}\right)^{1/2} \left(\frac{R}{10\,\mathrm{km}}\right)^{-3/2} , \tag{23}$$

---

[9] Valid for $\beta > 0.1$ and maximum NS mass $\geq 1.97\,\mathrm{M}_\odot$.

where M and R refer to the non-rotating configuration, then the maximum spin energy of a NS can be expressed, in terms of equations (22) and (23), as

$$E_{\rm spin,max} = 4.6\times 10^{52}\left(\frac{M}{{\rm M}_\odot}\right)^2\left(\frac{R_*}{10\,{\rm km}}\right)^{-1} \left(0.247+0.642\beta+0.466\beta^2\right)\ {\rm erg}. \qquad (24)$$

The maximum NS mass is $\gtrsim 2\,{\rm M}_\odot$ (Antoniadis et al. 2013): thus, $E_{\rm spin,\,max}$ can range from $\lesssim 3\times 10^{52}$ erg, for a $M = 1.4\,{\rm M}_\odot$, $R = 12$ km NS, to $\sim 10^{53}$ erg in extreme cases.

The two torques described in Section 3.4.2 draw spin energy and channel it into the EM and GW windows, respectively. Equation (19) gives the initial spin-down time due to magnetic dipole emission, $\tau_{\rm em} \sim 1.7\,{\rm d}\,P^2_{i,{\rm ms}} B^{-2}_{{\rm d},14}\left(1+\sin^2\chi\right)^{-1}$, P_i being the birth spin period. From equation (20), we get the GW-driven spin-down time, $\tau_{\rm GW}\sim 3.3\,{\rm d}\,P^4_{i,{\rm ms}}\epsilon_B^2\hat{F}(\chi)^{-1}$. Given the large spin energy reservoir and short time-scales involved, bright EM and/or GW transients may occur when a highly magnetised, millisecond spinning NS is formed. The initial conditions determine the relative strengths of the EM and GW spin-down luminosities.

The solutions for $\chi(t)$ and $\Omega(t)$ from Section 3.4.2 are needed in order to calculate spin-down luminosities as a function of time in both the GW and EM window (equations 19 and 20); in this way, it is possible characterize both types of transients and determine their detectability.

4.1 GW transient signals

Our numerical solutions for $\chi(t)$ extend the analytical results of Dall'Osso et al. (2009). On the one hand they confirm that, for a large portion of parameter space, efficient GW emission is favored by the tilt angle quickly attaining large values (>60°), before the NS spin energy can be drained by EM torques. On the other hand, they reveal that bulk viscous dissipation will drop faster than previously calculated, limiting the growth of the tilt angle at large ϵ_B, despite the larger bulk viscosity coefficient calculated here. In particular, if[10] $\epsilon_{B,\,-3}\gtrsim 5$, the tilt angle remains small and, accordingly, the GW emission efficiency has a sharp drop.

To update earlier results on the strength and detectability of the expected GW signals, we first estimate the signal-to-noise ratio (S/N) for a one-detector ideal match-filtered search (e.g. Owen & Lindblom 2002). The orientation- and position-averaged strain is (Finn & Chernoff 1993)

$$h_a^2(f) = \frac{2\pi^4 G^2 I^2\epsilon_B^2}{5c^8 D^2} f^4\hat{F}(\chi), \qquad (25)$$

where $f = \Omega/\pi$ is the GW signal frequency and D the source distance. The S/N is thus

$$S/N = 2\sqrt{\int\frac{\tilde{h}_a^2(f)}{S_h(f)}df}. \qquad (26)$$

In equation (26), $\tilde{h}(f)$ is the Fourier transform of the instantaneous strain, and $S_h(f)$ the one-sided noise spectral density of the detector. For Advanced LIGO/Virgo, we adopted the design sensitivity curve[11] of Abbott et al. (2017b).

Detection by Advanced LIGO/Virgo – We calculated equation (26) in the case of EoS *II*, for two values of the NS magnetic moment, two combinations of the NS mass and radius, and adopting a standard distance of 20 Mpc. Results are shown in Fig. 4 (see caption for details). The GW signals last from ∼ a few hours up to $\gtrsim$a day (depending on the values of $P_{\rm ms}$, ϵ_B, and $B_{\rm d}$), during which the frequency decreases by a factor ∼2–3. S/N-values in Fig. 4 were calculated by integrating the signals for the first 12 h after the NS is born. We verified that, for the weaker signals, increasing the time span up to ∼24 h can result in a ∼25 per cent gain in S/N, while for the most powerful events the signal is concentrated in less than 12 h (our results are thus somewhat conservative for the lower-S/N signals).

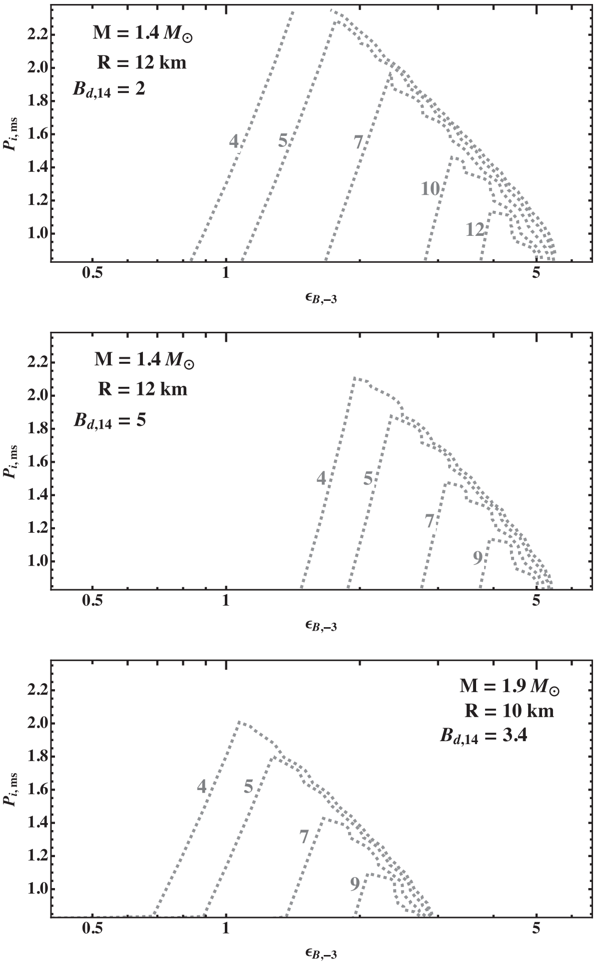

Figure 4. The orientation- and position-averaged S/N of a newborn magnetar at 20 Mpc, for EoS *II* and a single-detector matched-filter search, as a function of $P_{\rm ms}$ and ϵ_B. Signals are integrated for $\Delta t = 12$ h. We adopted two different values of the magnetic dipole moment and two choices of the NS mass and radius (see plots). In the upper and lower panels, the same value of $\mu_{32} = 1.7$ is used: different values of $B_{\rm d}$ reflect different NS radii. The positive slope side of the contours reflects magnetars whose tilt angle becomes quickly ∼90°: they efficiently emit GWs with a strain $\propto\epsilon_B$. The negative slope side corresponds to sources in which cooling freezes spin-flip before the tilt angle becomes large: they emit GWs with lower efficiency, which drops at higher ϵ_B.

Fig. 4 shows that a stronger $B_{\rm d}$ reduces the detectable region in parameter space and shifts it towards larger ϵ_B, as it increases the EM over the GW torque. Increasing the NS mass has a comparable effect, but shifts the detectable region to lower ellipticities. This results from the combination of a larger moment of inertia, which slightly favors the GW over the EM torque, and of

---

[10] The exact value depending also on the NS spin.

[11] Data files from https://dcc.ligo.org/LIGO-P1200087-v42.

incomplete flipping (see Fig. 3), which reduces the GW efficiency at larger ϵ_B.

Finally, for a fixed value of B_d, the maximum distance at which S/N is above a given threshold scales almost linearly with $1/P_{i,\,\rm ms}$ and ϵ_B. A sharp cut off in the maximum distance occurs for ϵ_B-values beyond the descending branch of the S/N curves in Fig. 4.

The long duration and strong spin-down of these *time-reversed* 'chirps' pose new technical challenges, not fully addressed by current detection algorithms. While a complete discussion of these problems is clearly beyond the scope of this work, we summarize them here, in order to assess realistic perspectives for signal detection.

Even with match-filtering, actual signal searches with unknown phase parameters have an F-statistics maximum S/N that is a factor $\sqrt{2}$ lower than the optimal value of equation (26) (Equations. 31, 64, and 112 in Jaranowski & Królak 2000). In reality, the search for these GW signals will be limited by available computing power, and will have to be carried out by using sub-optimal methods, leading to a further loss of sensitivity (e.g. Thrane et al. 2011, Prix, Giampanis & Messenger 2011, Coyne, Corsi & Owen 2016). In a semicoherent search, short data sets can be analyzed coherently and then combined incoherently to increase sensitivity. However, this is less sensitive than a coherent search by a factor $\sim N^{-1/4}$, where $N = T_{\rm obs}/T_{\rm short}$ is the number of short data sets in which the whole observation is split. The potential of these methods can be enhanced in an hierarchical scheme, in which candidate events are followed up with increasingly selective criteria and a finer tiling in a smaller region of parameter space. As a specific example, we assumed a search done with the frequency Hough-transform, which extends the existing calculations for continuous waves (Astone et al. 2014) to periodic signals slowing down on a $\sim 10^4$–10^5 s time-scale (Miller et al., in preparation). We adopted $\epsilon_{B,\,-3} \sim 1$, $I_{45} = 1.4$, an initial spin period of 1 ms, $T_{\rm shor} \lesssim 100$ s and standard values for (i) the threshold on the critical ratio for candidate selection on the Hough map ($\mathrm{CR_{thr}} \sim 5$), which sets the false alarm probability; (ii) the threshold for peak selection on the equalized power spectra $\theta_{\rm thr} = 2.5$ (see Astone et al. 2014). The loss in sensitivity translates into a factor ~5–6 smaller range with respect to the value adopted in Fig. 4 (Miller et al., in preparation).

Detection by the ET – The sensitivity of third generation detectors, like the Einstein Telescope (ET), will improve significantly over that of Advanced LIGO/Virgo. In the ET-D configuration, for example, $S_0 \approx 3.6 \times 10^{-49}\,\mathrm{Hz}^{-1}$ at 1 kHz (Abbott et al. 2017c) and a sensitivity gain by a factor of ~8 can be anticipated. Therefore, the curves of Fig. 4 would hold for a distance of ~160 Mpc, whereas taking into account the sensitivity loss of semicoherent searches, the corresponding range would become ~25–30 Mpc.

Expected event rate – Millisecond spinning magnetars may be formed either in the core-collapse (CC) of massive stars or in binary NS mergers. Li et al. (2011) estimate a rate $\sim 0.7 \times 10^{-4}\,\mathrm{yr}^{-1}\,\mathrm{Mpc}^{-3}$ for all CC SNe in the local Universe. To average out local overdensities, we integrate the rate over 60 Mpc, within which ~65 CC SNe per year are expected. Using the cumulative blue light distribution in the local universe (Kopparapu et al. 2008; Abadie et al. 2010) as a proxy for the star formation rate, the above translates to a magnetar birth rate of (i) $\gtrsim 0.3\,\mathrm{yr}^{-1}$ within 20 Mpc, if they represent $\gtrsim$10 per cent of all NSs formed in CC SNe (note that Stella et al. 2005 estimated $\lesssim 1\,\mathrm{yr}^{-1}$, based on the energetics of magnetar Giant Flares); (ii) $\gtrsim 0.01\,\mathrm{yr}^{-1}$ within 4 Mpc, the sub-optimal horizon for Advanced LIGO/Virgo; and (iii) $\sim(0.5$–$1)\,\mathrm{yr}^{-1}$ within 25–30 Mpc, the estimated range of third generation detectors.

Newborn magnetars formed in BNS mergers could either be stable objects, or supra/hyper-massive NS bound to collapse to BHs after loosing some of their centrifugal support (e.g. Giacomazzo & Perna 2013). In the latter case, their GW signals, albeit shorter lived, may be especially rich of information about the NS EoS (Dall'Osso et al. 2015; Piro, Giacomazzo & Perna 2017). In the former case, the signal would be slightly stronger than calculated here – because the NS is close to the maximum mass – and would thus allow for a somewhat larger horizon, $\lesssim$40 Mpc with third generation detectors (adopting the numbers from Dall'Osso et al. 2015, and factoring in the sensitivity loss of realistic searches, as discussed above). The event rate for BNS mergers is estimated to be ~(320–4700) $\mathrm{Gpc}^{-3}\,\mathrm{yr}^{-1}$ (Chruslinska et al. 2018, and references therein), implying a rate $\sim(0.9$–$13) \times 10^{-4}\,\mathrm{yr}^{-1}$ within the sub-optimal horizon for Advanced LIGO/Virgo, and $\sim(0.09 - 1.3)\,\mathrm{yr}^{-1}$ within the sub-optimal horizon for third generation detectors (see e.g. Dall'Osso et al. 2015, Piro et al. 2017, for a discussion of the fraction of BNS mergers that may produce stable/supra-massive NSs). In the latter case, the stronger 'chirp' from the inspiral would serve as a trigger for a targeted search of the signal emitted by the newly formed NS.

4.2 EM transients

The GW signals from magnetars born in CC are expected to be associated to SN explosions (e.g. Thompson & Duncan 1993, Gaensler, Gotthelf & Vasisht 1999). Within the ranges estimated in Section 4.1 for Advanced and third generation interferometers, these SNe would be easily identified in the optical/NIR. This makes prospects for multimessenger studies of such GW events especially promising. For magnetars originating from binary NS mergers, the same two types of EM counterparts predicted for the merger are expected: a prompt, short GRB for favorable viewing angles (e.g. Eichler et al. 1989) and/or a kilonova on a time-scale ~day, for a wide range of viewing angles (e.g. Li & Paczyński 1998, Metzger 2017; Arcavi et al. 2017, Cowperthwaite et al. 2017, Kasen et al. 2017).

The NS spin energy may contribute powering the SN or other phenomena, if magnetic dipole spin-down is dominant, as extensively discussed in the literature. Magnetars formed in CC may lead to the production of a long-GRB (e.g. Thompson, Chang & Quataert 2004, Bucciantini et al. 2006, Metzger et al. 2007, 2011), a shallow decay phase in the GRB early afterglow (e.g. Zhang & Mészáros 2001, Dall'Osso et al. 2011, Bernardini et al. 2012), or a Super-Luminous Supernova (SLSN; Kasen & Bildsten 2010, Greiner et al. 2015). The spin energy of a magnetar formed in a binary NS merger may power the extended emission following (some) short GRBs (Metzger, Quataert & Thompson 2008, 2011). The coexistence of a GW torque has not been considered yet in any of such scenarios; however, GW-driven spin-down was considered by, for example, Dall'Osso & Stella 2007 and Dall'Osso et al. 2009, in relation to the energetics of SN remnants associated to galactic magnetars. We plan to address this issue in greater detail in a future study.

5 CONCLUSIONS

We improved on previous work on the role of the spin-flip instability in the GW emission from newborn magnetars, by: (i) calculating the coefficient of bulk viscosity, the dissipative process driving the instability, for $npe\mu$ matter, with various realistic EoS's;

(ii) introducing a prescription for the way in which fluid compressibility drops as the cooling NS switches between the low- and high-frequency limits of bulk viscosity; and (iii) deriving the first self-consistent solution of the coupled evolution equations for the NS tilt angle ('spin-flip') and spin frequency, under the effect of bulk viscous dissipation, and of GW and EM spin-down torques. Based on that, we calculated the detectability of the GW signal with Advanced LIGO/Virgo and future third generation detectors, as a function of the magnetically-induced ellipticity and initial spin period of the NS.

Our main conclusions are: (i) the bulk viscosity coefficient of NS matter with a realistic EoS and chemical composition is, in general, larger than the standard expression valid for pure *npe* matter. This makes bulk viscous dissipation more efficient than previously calculated, and the 'spin-flip' instability accordingly faster; (ii) the 'spin-flip' instability freezes, and the tilt angle stops growing, as the NS cools below $\sim$(8–9) × 10^9 K, due to the decreasing compressibility of the $npe\mu$ fluid. (iii) at spin periods $\lesssim$2 ms, spin-flip will cause a fast growth of the tilt angle χ, in turn, causing strong GW emission. At large ellipticities, on the other hand, the tilt angle growth time is proportionally longer, and spin-flip freezes before χ has evolved significantly. We find that, for $\epsilon_{B,-3} \gtrsim 5$, GW emission is quenched because the tilt angle remains close to its (small) initial value; (iv) in realistic data analyses with sub-optimal sensitivity, Advanced LIGO/Virgo-class detectors can capture the GW signal of a millisecond spinning, magnetically distorted NS up to a distance $\sim$(3–4) Mpc $\epsilon_{B,-3}/\mathrm{P}_{\mathrm{ms}}$, provided that the dipole B-field is $\mathrm{B}_{\mathrm{d}} \lesssim 3 \times 10^{14}$ G. Magnetars are expected to form in $\gtrsim$10 per cent of CC SNe, implying one event per $\sim$30–100 yr within that distance range. (v) Third-generation interferometers, with a sensitivity improved by a factor $\sim$8 in the relevant frequency range, will push the horizon of even sub-optimal searches to >30 Mpc, within which an event rate $\gtrsim$(0.5–1) yr^{-1} can be expected. In addition, this expanded horizon would likely include an interesting number of BNS mergers ($\sim$0.09–1.3) yr^{-1} according to current best estimates), increasing the chances of detecting magnetars formed in binary NS mergers, the exact rate of which depends on the uncertain fraction of mergers that can produce a stable, or long-lived, NS.

For magnetars formed in the CC of massive stars, the accompanying optical/NIR SN should be easily detectable within the horizon of Advanced and third generation interferometers, leading to a robust association between the GW signal and the EM counterpart. For magnetars formed in BNS mergers, an optical/NIR kilonova emission should be expected for most viewing geometries, along with a (short) γ-ray burst for a favourable viewing angle and/or for sufficiently small distances, as the event GW170817 has demonstrated (e.g. Abbott et al. 2017e; Coulter et al. 2017, Arcavi et al. 2017; Alexander et al. 2018). The spin energy of a millisecond NS can provide additional power to the EM emission of these events, in a manner similar to that discussed for, for example, long-GRBs and SLSNe. In all cases, detection of the characteristic GW *time-reversed* 'chirp' associated to a newborn magnetar would give an unambiguous confirmation of the nature of the central engine. The development of much-needed search algorithms and strategies for the detection of such signals is urged.

ACKNOWLEDGEMENTS

SD acknowledges support from National Science Foundation (NSF) award AST-1616157. LS acknowledges financial contribution from agreement ASI-INAF I/037/12/0.

REFERENCES

Abadie J. et al., 2010, Class. Quantum Gravity, 27, 173001
Abbott B. P. et al., 2016, Phys. Rev. Lett., 116, 061102
Abbott B. P. et al., 2017a, Phys. Rev. Lett., 118, 221101
Abbott B. P et al., 2017b, Living Rev. Relativ., 21, 3
Abbott B. P. et al., 2017c, Class. Quantum Gravity, 34, 044001
Abbott B. P. et al., 2017d, Phys. Rev. Lett., 119, 161101
Abbott B. P. et al., 2017e, ApJ, 848, L12
Akgün T., Reisenegger A., Mastrano A., Marchant P., 2013, MNRAS, 433, 2445
Akmal A., Pandharipande V. R., Ravenhall D. G., 1998, Phys. Rev. C, 58, 1804
Alexander K. D. et al., 2018, preprint (arXiv:1805.02870)
Antoniadis J. et al., 2013, Science, 340, 448
Arcavi I. et al., 2017, Nature, 551, 64
Astone P., Colla A., D'Antonio S., Frasca S., Palomba C., 2014, Phys. Rev. D, 90, 042002
Bernardini M. G., Margutti R., Mao J., Zaninoni E., Chincarini G., 2012, A&A, 539, A3
Bonazzola S., Gourgoulhon E., 1996, A&A, 312, 675
Braithwaite J., 2009, MNRAS, 397, 763
Bucciantini N., Thompson T. A., Arons J., Quataert E., Del Zanna L., 2006, MNRAS, 368, 1717
Chruslinska M., Belczynski K., Klencki J., Benacquista M., 2018, MNRAS, 474, 2937
Ciolfi R., Rezzolla L., 2013, MNRAS, 435, L43
Corsi A., Mészáros P., 2009, ApJ, 702, 1171
Coulter D. A. et al., 2017, Science, 358, 1556
Cowperthwaite P. S. et al., 2017, ApJL, 848, L17
Coyne R., Corsi A., Owen B. J., 2016, Phys. Rev. D, 93, 104059
Cutler C., 2002, Phys. Rev. D, 66, 084025
Dall'Osso S., Perna R., 2017, MNRAS, 472, 2142
Dall'Osso S., Stella L., 2007, Ap&SS, 308, 119
Dall'Osso S., Shore S. N., Stella L., 2009, MNRAS, 398, 1869
Dall'Osso S., Stratta G., Guetta D., Covino S., De Cesare G., Stella L., 2011, A&A, 526, A121
Dall'Osso S., Giacomazzo B., Perna R., Stella L., 2015, ApJ, 798, 25
Demorest P. B., Pennucci T., Ransom S. M., Roberts M. S. E., Hessels J. W. T., 2010, Nature, 467, 1081
Eichler D., Livio M., Piran T., Schramm D. N., 1989, Nature, 340, 126
Finn L. S., Chernoff D. F., 1993, Phys. Rev. D, 47, 2198
Gaensler B. M., Gotthelf E. V., Vasisht G., 1999, ApJ, 526, L37
Giacomazzo B., Perna R., 2013, ApJ, 771, L26
Greiner J. et al., 2015, Nature, 523, 189
Haensel P., Levenfish K. P., Yakovlev D. G., 2000, A&A, 357, 1157
Haensel P., Levenfish K. P., Yakovlev D. G., 2001, A&A, 372, 130
Ipser J. R., Lindblom L., 1991, ApJ, 373, 213
Jaranowski P., Królak A., 2000, Phys. Rev. D, 61, 062001
Jones P. B., 1976, Ap&SS, 45, 369
Jones D. I., Andersson N., 2001, MNRAS, 324, 811
Kasen D., Bildsten L., 2010, ApJ, 717, 245
Kasen D., Metzger B., Barnes J., Quataert E., Ramirez-Ruiz E., 2017, Nature, 551, 80
Kopparapu R. K., Hanna C., Kalogera V., O'Shaughnessy R., González G., Brady P. R., Fairhurst S., 2008, ApJ, 675, 1459
Lander S. K., Jones D. I., 2017, MNRAS, 467, 4343
Lasky P. D., Glampedakis K., 2016, MNRAS, 458, 1660
Lattimer J. M., Prakash M., 2016, Phys. Rep., 621, 127
Li L.-X., Paczyński B., 1998, ApJ, 507, L59
Li W., Chornock R., Leaman J., Filippenko A. V., Poznanski D., Wang X., Ganeshalingam M., Mannucci F., 2011, MNRAS, 412, 1473
Lindblom L., Owen B. J., 2002, Phys. Rev. D, 65, 063006
Makishima K. et al., 2014, Phys. Rev. Lett., 112, 171102
Mastrano A., Melatos A., Reisenegger A., Akgün T., 2011, MNRAS, 417, 2288
Mestel L., Takhar H. S., 1972, MNRAS, 156, 419
Metzger B. D., 2017, Living Rev. Relativ., 20, 3

Metzger B. D., Thompson T. A., Quataert E., 2007, ApJ, 659, 561
Metzger B. D., Quataert E., Thompson T. A., 2008, MNRAS, 385, 1455
Metzger B. D., Giannios D., Thompson T. A., Bucciantini N., Quataert E., 2011, MNRAS, 413, 2031
Owen B. J., Lindblom L., 2002, Class. Quantum Gravity, 19, 1247
Page D., Geppert U., Weber F., 2006, Nucl. Phys. A, 777, 497
Page D., Prakash M., Lattimer J. M., Steiner A. W., 2011, Phys. Rev. Lett., 106, 081101
Piro A. L., Giacomazzo B., Perna R., 2017, ApJ, 844, L19
Prix R., Giampanis S., Messenger C., 2011, Phys. Rev. D, 84, 023007
Reisenegger A., Goldreich P., 1992, ApJ, 395, 240
Sawyer R. F., 1989, Phys. Rev. D, 39, 3804
Spitkovsky A., 2006, ApJL, 648, L51
Steiner A. W., Lattimer J. M., Brown E. F., 2010, ApJ, 722, 33
Stella L., Dall'Osso S., Israel G. L., Vecchio A., 2005, ApJ, 634, L165
Thompson C., Duncan R. C., 1993, ApJ, 408, 194
Thompson T. A., Chang P., Quataert E., 2004, ApJ, 611, 380
Thrane E. et al., 2011, Phys. Rev. D, 83, 083004
Zhang B., Mészáros P., 2001, ApJ, 552, L35

This paper has been typeset from a TEX/LATEX file prepared by the author.